J. Phys. Chem. C **2008,** *112,* 17281–17290

Accurate Simulation of Surfaces and Interfaces of Face-Centered Cubic Metals Using 12−6 and 9−6 Lennard-Jones Potentials

Hendrik Heinz,*,† R. A. Vaia,‡ B. L. Farmer,‡ and R. R. Naik‡

Department of Polymer Engineering, University of Akron, Akron, Ohio 44325, and Materials and Manufacturing Directorate, Air Force Research Laboratory, Wright Patterson Air Force Base, Ohio 45433

Received: March 5, 2008; Revised Manuscript Received: August 25, 2008

Molecular dynamics and Monte Carlo simulations often rely on Lennard-Jones (LJ) potentials for nonbond interactions. We present 12−6 and 9−6 LJ parameters for several face-centered cubic metals (Ag, Al, Au, Cu, Ni, Pb, Pd, Pt) which reproduce densities, surface tensions, interface properties with water and (bio)organic molecules, as well as mechanical properties in quantitative (<0.1%) to good qualitative (25%) agreement with experiment under ambient conditions. Deviations associated with earlier LJ models have been reduced by 1 order of magnitude due to the precise fit of the new models to densities and surface tensions under standard conditions, which also leads to significantly improved results for surface energy anisotropies, interface tensions, and mechanical properties. The performance is comparable to tight-binding and embedded atom models at up to a million times lower computational cost. The models extend classical simulation methods to metals and a variety of interfaces with biopolymers, surfactants, and other nanostructured materials through compatibility with widely used force fields, including AMBER, CHARMM, COMPASS, CVFF, OPLS-AA, and PCFF. Limitations include the neglect of electronic structure effects and the restriction to noncovalent interactions with the metals.

1. Introduction

Metals and alloys serve traditionally as load bearing structures, conductors, and materials for accessories. Recently, metallic nanostructures and their interfaces with biological molecules, surfactants, solvents, and organic matter have shown promise for application in sensors, optical, electronic, and biomedical devices. Examples include the surfactant-directed growth of metal nanostructures as well as the selective binding of peptides and specifically designed cell surfaces to metal nanoparticles.[1−5] The understanding of such nanometer-scale processes, the interpretation of experimental data, and the choice of suitable surface-surfactant combinations, alloys, and morphological features is often difficult and can be advanced through simulation.[6−8] Examples include the explanation of X-ray diffraction (XRD), dielectric, IR, sum frequency generation (SFG), UV, NMR, differential scanning calorimetry (DSC), atomic force microscopy (AFM), and transmission electron microscopy (TEM) data on the basis of simulation for some inorganic−organic hybrid materials such as organically modified layered silicates although rarely yet for metal-related interfaces.[8−17] Therefore, the present paper focuses on the introduction of suitable Lennard-Jones parameters for the accurate simulation of face-centered cubic (fcc) elemental metals and their nanometer-scale interfaces.

For the successful combination of experiment and simulation, the reliability of computational models and their compatibility with existing simulation tools are important. For systems containing elemental metals, models can be distinguished in three broad categories: (1) At the electronic structure level, tight-binding, density functional, or other quantum-mechanical methods can be employed for small clusters of metals and interfaces ($\sim 10^3$ atoms) to simulate dynamical processes on the order of picoseconds.[18,19] Average deviations in densities, surface, and mechanical properties range from 2 to 20% relative to experiment and are associated with uncertainty about the exact exchange-correlation functional as well as the treatment of relativistic effects in the presence of d and f electrons. (2) At a semiempirical level, embedded atom models (EAM) are available for larger assemblies ($\sim 10^4$ atoms) and longer simulation times.[20−22] Although the computational cost of this approach is lower, agreement with experiment is less satisfactory compared to the tight-binding approach. Particularly, surface energies are underestimated up to 50%,[19] and compatibility with existing semiempirical parameter sets (force fields) for organic molecules, polymers, and biomacromolecules is difficult to achieve. (3) At the classical mechanical level, Lennard-Jones (LJ) potentials[23−25] can be employed for substantially larger systems ($\sim 10^6$ atoms), and dynamical processes on a time scale up to 1 μs are accessible.[26,27] This is more than a million times faster than quantum-mechanical methods, and a variety of force fields for biological and organic molecules are available which include LJ parameters.[28−34] However, existing LJ potentials for metals have been poor approximations with deviations in surface and mechanical properties on the order of 100% relative to experiment under ambient conditions, and are thus often omitted in major force fields.[26,27]

We show that these discrepancies between model and experiment are related to physical misunderstanding of the LJ parameters for fcc metals and introduce accurate LJ parameters under ambient conditions that can be used with existing force fields for the simulation of metals and hybrid interfaces using molecular dynamics and Monte Carlo methods. The outline of the paper follows. In section 2, we discuss two common functional forms of the LJ potential, the physical interpretation, shortcomings of the existing parameters, and the integration into

---

* To whom correspondence should be addressed. E-mail: hendrik.heinz@uakron.edu.

† University of Akron.

‡ Wright Patterson Air Force Base.

10.1021/jp801931d CCC: $40.75

existing force fields using combination rules. In section 3, the new parameters are stated. In section 4, we describe computational methods for the evaluation of the density, surface, interface, and mechanical properties. In section 5, the computational results with the new LJ parameters are discussed in relation to experiment, existing LJ parameters, and other models. In section 6, the paper concludes with a summary and a preview of work in progress.

2. Functional Form and Physical Interpretation of the LJ Parameters

In the following, we discuss two common functional forms of the LJ potential, the interpretation of the LJ parameters for homoatomic fcc metals, shortcomings of earlier models, and the integration of the new LJ models into existing force fields using combination rules.

2.1. Functional Form. LJ potentials are often used in the 12−6 form and in the 9−6 form;[26−34] although other combinations of exponents can also be meritorious.[23−26,35−37] For example, a 12−6 LJ potential is employed in the force fields AMBER,[30] CHARMM,[32] CVFF,[28,34] OPLS-AA,[31] and a 9−6 LJ potential is employed in the force fields COMPASS[33,34] and PCFF:[29,34]

$$E = \varepsilon_0\left[\left(\frac{r_0}{r}\right)^{12} - 2\left(\frac{r_0}{r}\right)^{6}\right] = \frac{A}{r^{12}} - \frac{B}{r^{6}}$$

$$A = \varepsilon_0 r_0^{12} \qquad B = 2\varepsilon_0 r_0^{6} \qquad r_0 = \sqrt[6]{\frac{2A}{B}} \quad (1)$$

$$E = \varepsilon_0\left[2\left(\frac{r_0}{r}\right)^{9} - 3\left(\frac{r_0}{r}\right)^{6}\right] \quad (2)$$

In eqs 1 and 2, ε_0 represents the equilibrium nonbond energy and r_0 the equilibrium nonbond distance between two atoms of the same type (Figure 1). In mixtures with other elements or compounds, the parameters $\varepsilon_{0,ij}$ and $r_{0,ij}$ for nonbond interactions between different atom types i and j can be obtained by combination rules as discussed in section 2.3.[28−34,38−42]

2.2. Physical Interpretation for the Pure Metals. Equations 1 and 2 show that every pure fcc metal is characterized by only two adjustable parameters r_0 and ε_0 in the LJ model which physically represent the density and the surface free energy at a given point in the phase diagram.[13] This interpretation of the parameters is justified (1) by the density as a volumetric quantity and (2) by surface properties as an essential driving force in self-assembly processes at interfaces.[1−8] Both quantities should thus be reproduced as accurately as possible. Moreover, (3) LJ models as well as many other molecular models cannot cover a temperature range of several thousand Kelvin (boiling points of metals) and extreme pressure without adjustments to the parameters. Therefore, a reference state is necessary, and we chose ambient conditions with a temperature of 298.15 K and a pressure of 101.325 kPa as a reference point to experiment, which is suitable for many condensed matter applications and compatible with various force fields. The rationale of this approach has been described by Heinz et al.[13] in a more general form including charged systems and shows promise for the accurate parametrization of force fields of inorganic as well as organic solids.

We note that this strategy to derive LJ parameters for metals differs from common approaches for nonpolar organic liquids.[28−33,43,44] In one such approach,[28−33] computed densities and vaporization energies (cohesive energies) are brought in agreement with experimental data.[28−33] If the boiling point lies approximately within ±200 K of room temperature, the well-reproduced cohesive energy in the model for the liquid also leads to surface and interface properties in good agreement with experiment under ambient conditions because LJ parameters typically perform reliably in this temperature range without further adjustments. The approach cannot be applied to metals and minerals,[13] however, because high melting and boiling points up to 4000 K[45,46] exceed the acceptable temperature range near 298 K by more than an order of magnitude. Thus, vaporization energies are not suitable to parametrize a LJ model for metals at room temperature. In another strategy for nonpolar liquids,[43,44] critical points in experimental phase diagrams, such as temperature vs density, are considered as reference points to assign LJ parameters. This approach is also not suitable for fcc metals at room temperature because the reference state is strongly substance-dependent and located in regions of the phase diagram up to 8000 K.[46]

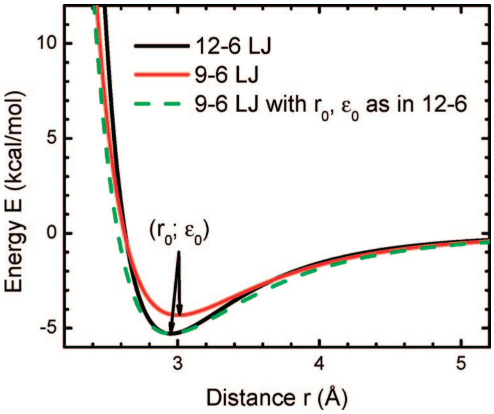

Figure 1. Comparison of the 12−6 LJ potential and the equivalent 9−6 LJ potential (shown for Au). When the values of r_0 and ε_0 in the 12−6 potential would be transferred without modification to the 9−6 potential (dashed line), the computed density and the computed surface energy would increase.

In conclusion, the density[46] and the surface tension[45] under standard conditions are suitable reference points to experiment. The accurate representation of the density, mainly determined by r_0, and of the surface free energy for the lowest energy {111} face, mainly determined by ε_0, increases the reliability of existing LJ parameters by an order of magnitude in comparison to parametrizations that rely on the density and on the vaporization energy. For example, the resulting LJ model for fcc metals is also capable of the nearly quantitative analysis of surface energies of other crystal faces as well as interfacial energies with water and (bio)organic molecules. Elastic moduli can be computed in ±20% agreement with experiment using 12−6 LJ parameters and with −35% systematic deviation from experiment using 9−6 LJ parameters, down from deviations of up to several multiples otherwise (section 5).

We emphasize these approaches to assign LJ parameters because earlier LJ parameters for metals[26] and combinations of LJ parameters with many-body terms[27] relied on vaporization energies at 2000−4000 K for the assignment of ε_0 and considerable difficulties to bring cohesive energies, surface energies, and elastic moduli in agreement with experiment at room temperature were consequently reported. The discrepancy between computed vs measured surface and mechanical properties reached multiples relative to experiment,[26,27] and it was assumed that alternative models may hold more promise, even though EAM models exhibit deviations in surface tensions on the order of 50%.[19−22] As a result, most force fields do not contain LJ parameters for elemental metals and some force fields

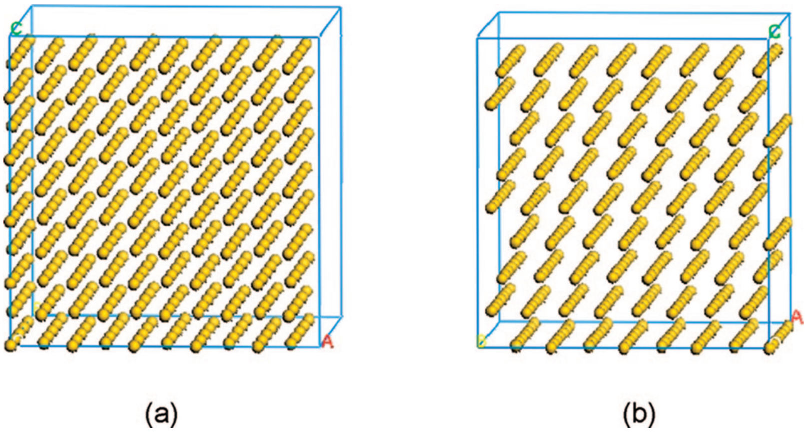

Figure 2. (a) Model of a cubic Au 5 × 5 × 5 super cell. {100} cleavage planes can be generated perpendicular to the three Cartesian coordinate axes. (b) Model of an alternative orthorhombic super cell. {111} cleavage planes can be generated perpendicular to the vertical axis.

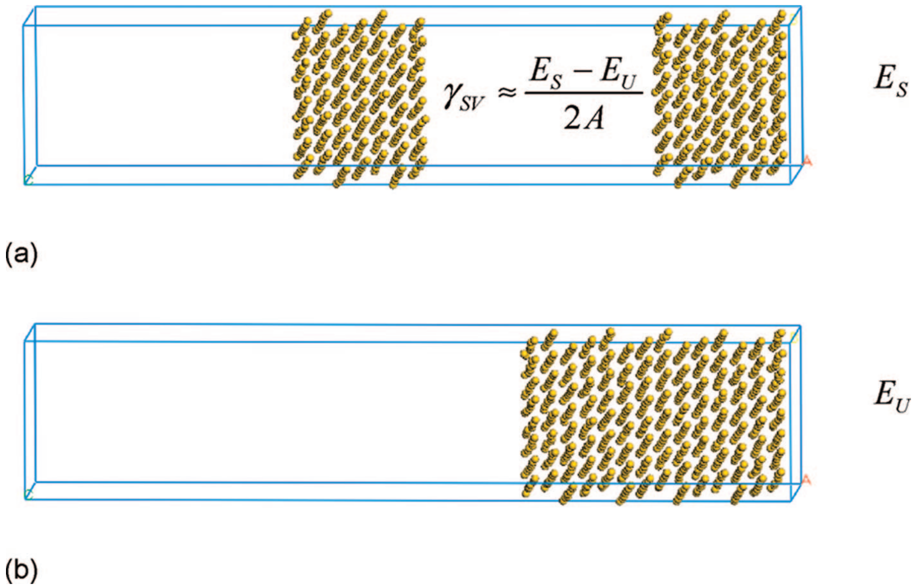

Figure 3. Illustration of the calculation of the surface tension for a {111} surface using two boxes with (a) separated surfaces and (b) unified surfaces.

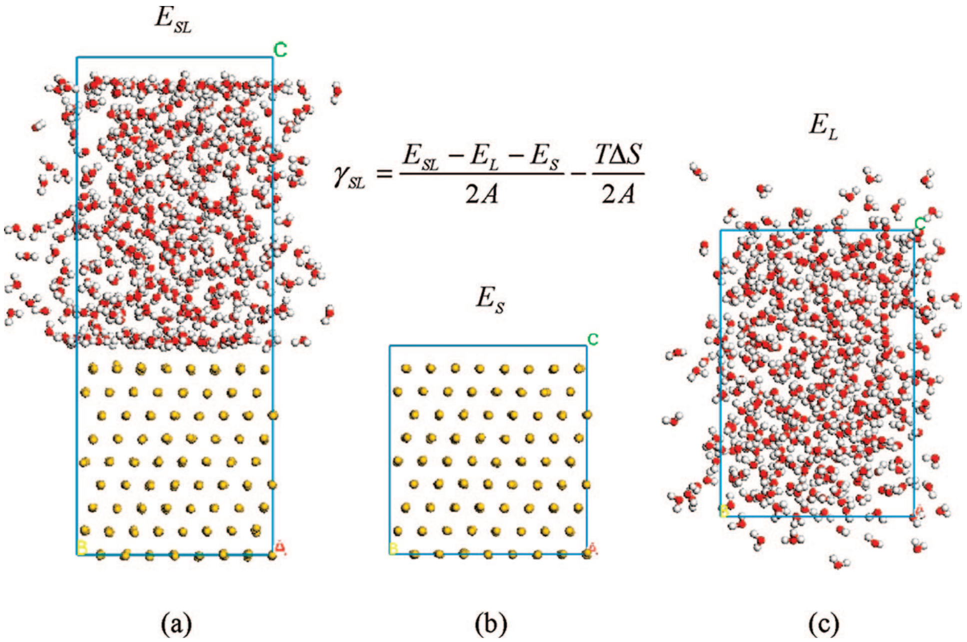

Figure 4. Illustration of the calculation of the metal−water interface tension using three boxes with (a) a metal−water interface, (b) pure metal, and (c) pure water.

TABLE 1: New 12−6 and 9−6 LJ Parameters for fcc Metals

	12−6 LJ potential (AMBER, CHARMM, CVFF, OPLS-AA)[a]				9−6 LJ potential (COMPASS, PCFF)[b]	
metal	r_0 (Å)	ε_0 (kcal/mol)	A (kcal/mol × Å^{12})	B (kcal/mol × Å^6)	r_0 (Å)	ε_0 (kcal/mol)
Ag	2.955	4.56	2021000	6072	3.005	3.73
Al	2.925	4.02	1577000	5035	2.976	3.26
Au	2.951	5.29	2307000	6987	3.003	4.32
Cu	2.616	4.72	484800	3026	2.661	3.84
Ni	2.552	5.65	431100	3121	2.598	4.59
Pb	3.565	2.93	12350000	12030	3.622	2.47
Pd	2.819	6.15	1549000	6173	2.868	5.03
Pt	2.845	7.80	2193000	8272	2.896	6.38

[a] Equation 1. [b] Equation 2.

TABLE 2: Cell Parameters for a $(5a)^3$ Super Cell in Experiment and in the Simulation (Ångstroms)

metal	exptl[a]	new 12−6	new 9−6	old 12−6[b]	old 9−6[c]
Ag	20.4285	20.434	20.427	20.470	20.528
Al	20.248	20.244	20.249	20.275	20.386
Au	20.391	20.389	20.391	20.452	20.455
Cu	18.073	18.080	18.072	18.085	18.185
Ni	17.620	17.620	17.621	17.640	17.696
Pb	24.751	24.762	24.750	24.813	24.719
Pd	19.4515	19.461	19.452	19.495	19.521
Pt	19.618	19.622	19.620	19.646	19.646
Stddev to Expt	±0.001	±0.007	±0.001	±0.043	±0.091

[a] Reference 46. [b] CVFF. [c] COMPASS and PCFF (ref 55).

(CVFF, PCFF, COMPASS) contain parameters similar to refs 26 and 27, which have undergone empirical refinement over time. It is essential to realize that the poor performance of the existing LJ models at room temperature was associated with unsuitable reference states at 2000−4000 K and ambiguity in the physical interpretation. Therefore, we suggest the revision of prior conclusions on the suitability of LJ parameters for the simulation of fcc metals.

2.3. Integration into Existing Force Fields Using Combination Rules. The two parameters r_0 and ε_0 can be directly implemented in force fields which use a LJ potential and will lead to the same computed equilibrium density and surface tension of cleavage planes of the pure fcc metals. In addition, combination rules to derive the parameters $\varepsilon_{0,ij}$ and $r_{0,ij}$ for nonbond interactions between different atom types i and j offer a convenient pathway to unite the LJ parameters for fcc metals with a broad range of existing parameters for inorganic, organic, and biological compounds for the simulation of hybrid materials and interfaces. The most important condition for a successful combination hereby is the quality of the parameters for the added inorganic and (bio)organic species though; in addition, the suitability of combination rules also plays a role.[28−33] The influence of combination rules on the results is typically minor;[38−42] however, it is clear that combination rules between any atom types are approximations.

Therefore, we summarize the possible factors which have an influence in the simulation of hybrid systems and state our assumptions. (1) Actual force field parameters are approximations and can differ from one force field to another, such as different water models (SPC, TIP3P, and TIP5P). Even when combination rules and 1−4 scaling are identical, differences in force field parameters will change the computed properties of metal interfaces in proportion to the difference in parameters. Besides, the application of inadequately short cutoffs (10 Å) and coarse treatments of Coulomb interactions leads to different results,[38−40] which can be avoided and will not be considered further. (2) We assume a geometric mean for the 12−6 potential, $r_{0,ij} = (r_{0,ii}r_{0,jj})^{1/2}$ and $\varepsilon_{0,ij} = (\varepsilon_{0,ii}\varepsilon_{0,jj})^{1/2}$, as in AMBER, CVFF, and OPLS-AA, as well as a sixth power combination for the 9−6 potential, $r_{0,ij} = ((r_{0,ii}^6 + r_{0,jj}^6)/2)^{1/6}$ and $\varepsilon_{0,ij} = (\varepsilon_{0,ii}\varepsilon_{0,jj})^{1/2}[2r_{0,ii}^3 r_{0,jj}^3/(r_{0,ii}^6 + r_{0,jj}^6)]$, as in COMPASS and PCFF. In a system with multiple atom types characterized by sets of parameters r_0 and ε_0, a change in combination rules thus leads to different total energy. As an example, the 12−6 LJ potential of CHARMM calculates $r_{0,ij}$ as an arithmetic mean $r_{0,ij} = (r_{0,ii} + r_{0,jj})/2$ and employs the same geometric mean as in AMBER, CVFF, and OPLS-AA $\varepsilon_{0,ij} = (\varepsilon_{0,ii}\varepsilon_{0,jj})$, which causes a difference, albeit it is likely small. The quality of combination rules may be improved to a certain extent;[41] however, actual validation has been limited to relatively few systems and mostly resulted in quantitative and semiquantitative agreement with experiment. (3) Scaling schemes for nonbond interactions between 1−4 bonded atoms can have a remote impact on the energies of metal-hybrid interfaces since ideal values for r_0 and ε_0 for atoms with covalently bonded 1,4 connections depend on the extent of scaling of the 1−4 nonbond interactions (100%, 50%, etc) in the force field and affect the interaction with metal surfaces by means of combination rules. (4) Polarization effects also play a role on metal surfaces, as will be mentioned in section 5.

In conclusion, we consider the proposed LJ parameters for fcc metals independent from combination rules and from scaling of nonbond interactions between 1,4 bonded atoms since the validation involves only properties of the pure metal and only

TABLE 3: Solid−Vapor Surface Tension $\gamma_{\rm SV}^{\{111)}$ and $\gamma_{\rm SV}^{\{100\}}$ in Experiment and in the Simulation (in J/m^2)

	$\gamma_{\rm SV}^{\{111\}}$					$\gamma_{\rm SV}^{\{100\}}$		
metal	exptl[a]	new 12−6	new 9−6	old 12−6[c]	old 9−6[d]	exptl	new 12−6	new 9−6
Ag	1.32[b]−1.19	1.312	1.310	2.302	1.467	3−5% higher than $\gamma^{SV}_{(111)}$ (absolute values not known)[e]	1.383	1.343
Al	1.18[b]−1.10	1.185	1.176	2.671	1.204		1.234	1.213
Au	1.54[b]−1.48	1.540	1.539	2.963	2.174		1.609	1.580
Cu	1.77 ± 0.02[b]	1.767	1.761	3.540	1.772		1.836	1.807
Ni	2.24 ± 0.02[b]	2.225	2.234	4.744	2.486		2.323	2.276
Pb	0.567 ± 0.01	0.558	0.559	1.048	7.896		0.591	0.578
Pd	1.98 ± 0.02	1.980	1.994	3.166	2.410		2.062	2.040
Pt	2.46 ± 0.03	2.455	2.459	4.960	3.547		2.553	2.514
std dev to expt	±0.06	±0.008	±0.008	±1.79	±2.82		+4.5% relative to {111}	+2.6%

[a] All values from ref 45. [b] Direct measurement at 298 K, given in ref 45. The remaining values are extrapolated from different temperatures, with the stated reliability. [c] CVFF. [d] COMPASS and PCFF (ref 55). [e] Reference 56.

TABLE 4: Solid−Water Interface Tension $\gamma_{SL}^{\{111\}}$ in Experiment and in the Simulation (in J/m^2)

		$\gamma_{SL}^{\{111\}}$	
metal	exptl[a]	new 12−6[b]	new 9−6[c]
Ag	1.25[d]−1.12	1.04 ± 0.03	1.16 ± 0.03
Al	1.11[d]−1.03	0.95 ± 0.03	1.02 ± 0.03
Au	1.47[d]−1.41	1.24 ± 0.03	1.33 ± 0.03
Cu	1.70 ± 0.02[d]	1.47 ± 0.03	1.57 ± 0.03
Ni	2.17 ± 0.02[d]	1.84 ± 0.03	2.02 ± 0.03
Pb	0.494 ± 0.01	0.42 ± 0.03[e]	0.45 ± 0.03[e]
Pd	1.91 ± 0.02	1.63 ± 0.03	1.75 ± 0.03
Pt	2.39 ± 0.03	2.03 ± 0.03	2.18 ± 0.03
std dev to exptl	± 0.06	−14%	−8%

[a] Reference 58. [b] SPC water in CVFF. [c] SPC-like water in COMPASS (o2* and h1o). [d] On the basis of the direct measurement of $\gamma_{SL}^{\{111\}}$ at 298 K (see Table 3). [e] Because of the higher fluidity of the Pb−water interface in comparison to the other interfaces, an entropy correction of only +0.04 J/m^2 instead of +0.06 J/m^2 was applied (see section 4.3).

nonbond interactions. The incorporation of the LJ parameters in different force fields thus leads to the same density and surface tension of the fcc metals. Interfacial interactions with other metals, inorganics, and bio(organic) molecules depend on the quality of the force field parameters for these moieties, the suitability of given combination rules and 1−4 scaling conventions, as well as on polarization effects. In this paper, we limit ourselves to the two independent combination rules for CVFF and COMPASS (PCFF) for initial validation, which both demonstrate good compatibility with the LJ parameters for the metals and lead to improvements in interfacial energies up to an order of magnitude compared to previous parameters (section 5.3). Further quantitative validation of the effect of combination rules and 1,4 scaling will be provided in follow-up contributions.

3. New LJ Model for fcc Metals

Experimentally determined densities[46] and surface tensions of the low energy {111} surface are employed for the assignment of the parameters r_0 and ε_0 in the new LJ model at 298 K[2,45] under atmospheric pressure. The two parameters exhibit only minor interdependence in the final fit, which reflects the physically distinct roles. The new parameters are listed in Table 1 for the 12−6 and for the 9−6 LJ potentials. The values were derived from a least-squares fit; the number of significant digits is limited to computational accuracy within experimental uncertainty, and the models are valid within a temperature range of 298 ± 200 K. The comparison of 12−6 parameters and corresponding 9−6 parameters shows a systematic increase in r_0 by ~1.7% and a decrease in ε_0 by ~18% in the 9−6 potential which compensates for weaker repulsion and stronger attraction in the 9−6 potential (Figure 1).

This approach is very efficient since surface and interface properties of the metals determine the interaction with other components and are taken into account with the highest possible accuracy.[13] In the model, the metal consists of charge-neutral atoms with repulsive and dispersive van der Waals interactions according to eqs 1 or 2, respectively. Modifications for other temperatures (and pressures) are possible by adjustment of r_0 and ε_0.[47] Experimental values for the density and for the surface tension at a different temperature can be utilized to obtain modified parameters.[47]

4. Computational Methods

For the evaluation of the new and existing LJ models, we computed densities, surface tensions of the {111} and {100} faces, interface tensions with water, and isotropic elastic constants. The computational procedures are outlined in the following.

4.1. Density. Models of the fcc metals were constructed using lattice parameters derived from X-ray data.[46] Super cells of approximately 2 × 2 × 2 nm^3 size (5 × 5 × 5 unit cells) were employed to compute the equilibrium density using NPT molecular dynamics simulation under standard conditions (Figure 2a). Atmospheric pressure was maintained by the Parrinello−Rahman barostat with an isotropic stress of −0.1 MPa; the temperature was controlled at 298.15 K, and a spherical cutoff of LJ interactions at 1.2 nm was employed (see section 4.5). Changes in the trajectory were minimal after 100 ps, and an additional simulation time of 500 ps was sufficient to compute the average density with <0.1% deviation.

4.2. Surface Tension. Models of {111} and {100} cleavage planes were prepared from suitable super cells (Figure 2). Metal−vapor surface tensions γ_{SV} were computed on the basis of two NVT simulations, using models with and without two additional surfaces (Figure 3). The box dimensions correspond to multiples of the experimental cell parameters (Figure 2). A uniform metal slab of ~4 nm thickness and a vacuum slab of ~8 nm represent a unified surface; two separated metal slabs of half the thickness (~2 nm) and half the separation (~4 nm) represent a separated surface (Figure 3). Each of the two boxes was of the same dimensions for a given metal, contained the same total number of atoms, and was subjected to NVT molecular dynamics simulation at 298.15 K for 500 ps (Figure 3). The difference in average total energy between the separated structure E_S and the unified structure E_U equals the cleavage energy per surface area $2A$,[48] and the surface tension γ_{SV} follows as

TABLE 5: Isotropic Elastic Constants *E* (in GPa), *K* (in GPa), *G* (in GPa), and *ν* in Experiment and in the Simulation[a]

metal	Young's modulus *E* exptl,[b] 12−6, 9−6	bulk modulus *K* exptl,[b] 12−6, 9−6	shear Modulus *G* exptl,[b] 12−6, 9−6	Poisson ratio *ν* exptl,[b] 12−6, 9−6
Ag	**91.3**, 94, 59	**104**, 114, 76	**33.7**, 35, 21	**0.337**, 0.36, 0.37
Al	**70.7**, 84, 52	**75.9**, 104, 69	**26.3**, 31, 19	**0.345**, 0.365, 0.375
Au	**88.0**, 110, 70	**173**, 133, 90	**31.1**, 41, 26	**0.415**, 0.36, 0.37
Cu	**145**, 141, 87	**137**, 173, 118	**54.9**, 52, 32	**0.323**, 0.365, 0.375
Ni	**239**, 183, 114	**186**, 229, 153	**93.2**, 67, 41	**0.285**, 0.365, 0.375
Pb	**29.1**, 31, 20	**44.8**, 36, 27	**10.5**, 11, 7	**0.392**, 0.36, 0.37
Pd	**146**, 146, 90	**193**, 182, 122	**53.2**, 53, 33	**0.374**, 0.365, 0.375
Pt	**181**, 188, 117	**283**, 235, 154	**65.1**, 69, 42	**0.393**, 0.365, 0.375
std dev to exptl	± **3%**, Avg. +4% (±14%), Avg. −35% (±9%)	± **3%**, Avg. +4% (±23%) 30% (±15%)	± **3%**, Avg. +4% (±18%) 36% (±11%)	±0.005, ± 0.04 ±0.04

[b] References 46 and 53. Experimental results differ between independent sources up to a few percent at 298 K. [a] Every entry consists of the experimental value (bold), followed by the computed values using the new 12-6 and the new 9-6 LJ parameters.

$$\gamma_{\mathrm{SV}} = \frac{E_{\mathrm{S}} - E_{\mathrm{U}}}{2A} - T\frac{S_{\mathrm{S}} - S_{\mathrm{U}}}{2A} \approx \frac{E_{\mathrm{S}} - E_{\mathrm{U}}}{2A} \tag{3}$$

The entropy contribution $-T(S_{\mathrm{S}} - S_{\mathrm{U}})/2A$ is negligible compared to the cohesive energy contribution $(E_{\mathrm{S}} - E_{\mathrm{U}})/2A$ in the metals, supported by minor oscillations of the metal atoms around their lattice points in the bulk and at the cleaved surfaces.[49] Without approximation, the surface tension was also computed using the average in-plane pressure component $p_{\parallel} = (p_{xx} + p_{yy})/2$, the average vertical pressure component $p_{\perp} = p_{zz}$, and the vertical extension z_0 of the box during molecular dynamics simulation of the unified structure (Figure 3b)[50]

$$\gamma_{\mathrm{SV}} = \frac{(p_{\perp} - p_{\parallel})z_0}{2} \tag{4}$$

This method requires rather lengthy simulations to compute precisely $p_{\parallel}$ and $p_{\perp}$; nevertheless, results from eqs 3 and 4 were identical within ±10 mJ/m².

4.3. Interface Tension. Metal−water interface tensions $\gamma_{\mathrm{SL}}^{\{111\}}$ were computed similarly on the basis of three NVT simulations (Figure 4). A metal super cell of ~2 nm thickness with water molecules added onto the lowest energy {111} cleavage plane along the *z* coordinate represents the metal−water (SL) interface, a separate water slab of ~3 nm thickness represents the pure water (L), and a separate metal slab of ~2 nm thickness represents the pure metal (S) (Figure 4). All cells are based on multiples of the experimental cell parameters for the metal, a water density of 1 g/cm³, and were subjected to NVT molecular dynamics simulation at 298.15 ± 0.01 K for 500 ps. The SPC water model in CVFF (12−6 LJ potential) and an SPC-like water model in COMPASS (9−6 LJ potential) were employed using the combination rules described in section 2.3. The difference in average energies E_{SL}, E_{L}, and E_{S} yields the interfacial energy $(E_{\mathrm{SL}} - E_{\mathrm{L}} - E_{\mathrm{S}})/2A$, and the interface tension follows as:

$$\gamma_{\mathrm{SL}} = \frac{E_{\mathrm{SL}} - E_{\mathrm{L}} - E_{\mathrm{S}}}{2A} - T\frac{S_{\mathrm{SL}} - S_{\mathrm{L}} - S_{\mathrm{S}}}{2A} \tag{5}$$

The entropy contribution $(-T(S_{\mathrm{SL}} - S_{\mathrm{L}} - S_{\mathrm{S}})/2A)$ arises from the first layer of partially immobilized, superficial water (Figure 4) and was estimated from the melting enthalpy of ice (6.01 kJ/mol) at 273.15 K.[46] This corresponds to an entropy of freezing $\Delta S = -22$ J/(mol·K), and one layer of "frozen" water molecules on the metal surface in contact with water (45 molecules cover an area of ~4 nm²) leads to an entropy contribution +0.12 J/m². Becasue of significant residual mobility of this water layer during the simulation, unlike the frozen state, we assume an entropy contribution of +0.06 ± 0.03 J/m² in eq 5, equal to 50% of the total value. Without approximations, the interface tension for the metal−water box (Figure 4a) was also computed from eq 4 using more time-consuming calculations[50] and yields the same results as eq 5 within ±0.03 J/m². We do not assume polarization on the metal surface (see section 5).[51]

4.4. Elastic Moduli. The isotropic elastic constants Young's modulus *E*, bulk modulus *K*, shear modulus *G*, and the Poisson ratio *ν* were computed by static, dynamic, and fluctuation approaches[34] using a cubic supercell (Figure 2a). The static and the fluctuation approach yield the same moduli *E* and *K* within ±1−5% deviation using small strain in agreement with the definition[52,53] while large strain between 0.0 and 0.2 in the dynamic approach results in approximately +10% larger moduli. Results are quoted for the static and for the fluctuation approach at small strain. The values are identical to those derived from NPT simulation with a tensile stress $\sigma_{xx} = -p_{xx}$ between ±0.1 GPa and ±1 GPa along the *x* axis to calculate $E = E_{xx}$ (all other stresses zero) and with an isotropic stress $\sigma = -p_{xx} = -p_{yy} = -p_{zz}$ between ±0.1 GPa and ±1 GPa to calculate *K*. The reproducibility of the elastic moduli is within ±1−5%.

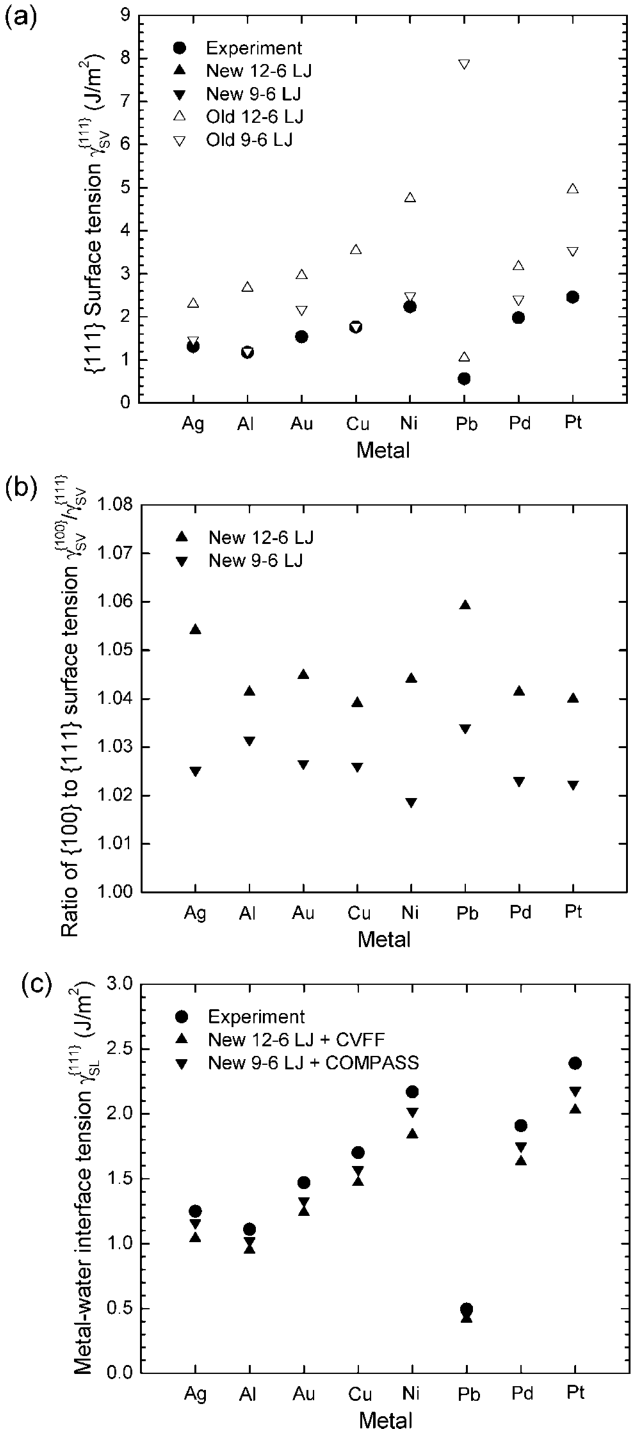

Figure 5. (a) Surface tension of the {111} face of the fcc metals in experiment as well as in the simulation with the new LJ models and with the existing LJ models. (b) Ratio of the surface tensions of the {100} face to the {111} face with the new LJ models. Experimental data indicate values between 1.03 and 1.05 but are yet uncertain for most metals.[56] (c) Metal−water interface tension of the {111} face in experiment and with the new LJ models incorporated in the CVFF and COMPASS force fields which contain SPC and SPC-like water models.

4.5. Visualization and Calculation Protocols. Visualization and calculations were performed using Materials Studio,[34] the Discover program,[34] and LAMMPS.[54] The simulation protocol

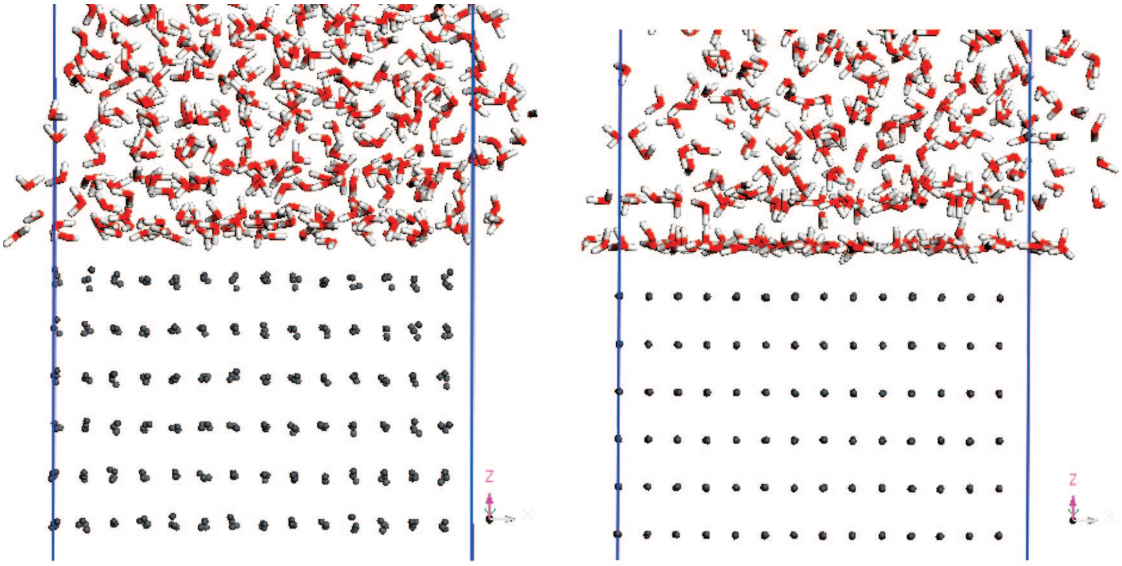

(a) (b)

Figure 6. Illustration of a metal−water interface (Pb-water as an example) with (a) new and (b) existing 9−6 LJ parameters in molecular dynamics simulation. When surface and interface tensions are highly overestimated as in part b, the first superficial water layer is virtually frozen, and only very small oscillations of the metal atoms in the lattice are seen.

for NVT molecular dynamics involved the Verlet integrator, a 12-Å cutoff for van der Waals interactions, Ewald summation with high accuracy (2.5×10^{-5} kcal/mol) for Coulomb interactions in the case of the solid−liquid interface, and a time step of 1 fs. The temperature was controlled with the Andersen thermostat (collision frequency between 0.05 and 1.0) at 298.15 K in Discover[34] and with the Nose−Hoover thermostat in LAMMPS.[54] An increase of the van der Waals cutoff from 12 to 15 Å resulted in a <1% increase in computed solid−vapor interface energies and a negligible change in density. Pressure control in NPT simulation was maintained using the Parrinello−Rahman barostat.

5. Results and Comparison with Experiment

In the following, we discuss the densities, surface tensions of the {111} and the {100} face, interface tensions with water, and the isotropic elastic constants obtained in the computation using the new 12−6 and 9−6 LJ parameters in comparison with experiment, existing LJ parameters, and other models. The data are presented in Tables 2, 3, 4, 5, as well as in Figures 5, 6, and 7. We consider the current parameter sets in the CVFF[28] (“Old 12−6”) and PCFF/COMPASS[29,33,55] (“Old 9−6”) force fields as existing parameters for the fcc metals, which have been empirically somewhat improved over earlier parameters in the literature.[26,27]

5.1. Density. Computed cell parameters (Table 2) and, consequently, the densities of the fcc metals are in quantitative agreement with experiment using both new and existing LJ models. The two parameters r_0 and ε_0 have been fitted to the density in the present and in earlier models as one of the two available reference points for each metal (section 2) so that the agreement between experiment and simulation is expected. A small difference of −1% between the computed and the experimental density ($\Delta\rho \sim [1 - (1 - \Delta a/a)^3]$) in the existing 9−6 LJ parameters is reduced to <0.1% in the new model.

5.2. Surface Tension. The most significant improvement of the models are the surface and interface energies. Solid−vapor interface tensions for the {111} faces are quantitatively fitted to experimental values with less than 1% deviation (Table 3 and Figure 5a). However, some experimental values for the {111} surface tension are uncertain in a ±5% range so that the LJ model is of the same ±5% reliability in these cases. Existing LJ parameters perform poor relative to experiment in most (but not all) cases, showing deviations up to several 100% (Figure 5a). In comparison to the LJ model, tight-binding[19] and embedded atom (EAM) models[19−22,27] are associated with typical deviations in surface energies of 15 and 50% to experiment, respectively, as well as computationally much more costly. Sometimes, even errors of multiples were reported.[27] Therefore, the new LJ model performs excellent in comparison to existing LJ models, EAM models, and even tight-binding methods.

For the {100} face, computed surface tensions are on average 4.5 or 2.6% higher than for the {111} face using 12−6 or 9−6 LJ potentials, respectively (Table 3 and Figure 5b). Experimental measurements of the surface energy anisotropy indicate that surface tensions of {100} faces are approximately 3−5% higher relative to {111} faces,[56] in support of the LJ model. However, the analysis of equilibrium nanoparticle shapes and the associated deduction of the anisotropy of the surface tension can be associated with significant errors so that experimental data are yet a semiquantitative guide.[56] The differences in surface tension between the {100} and {111} faces in the LJ model indicate a relation between the geometry of the metal surface and the surface energy, even though a dependence on the type of LJ potential is also seen.

5.3. Interface Tension. Experimental findings indicate that polar and nonpolar liquids wet clean metal surfaces with contact angles of 0°.[57,58] Computed metal−water interface tensions (Table 4) show a good fit with experimental values,[57,58] although some of the accuracy is compromised in comparison to pure metal surfaces (Figure 5c). The LJ model for the metal is employed in conjunction with an SPC water model (CVFF) and with an SPC-like water model (COMPASS) so that polarization effects, empirical assumptions in the force field, and combination rules introduce a systematic deviation on the order of −10%

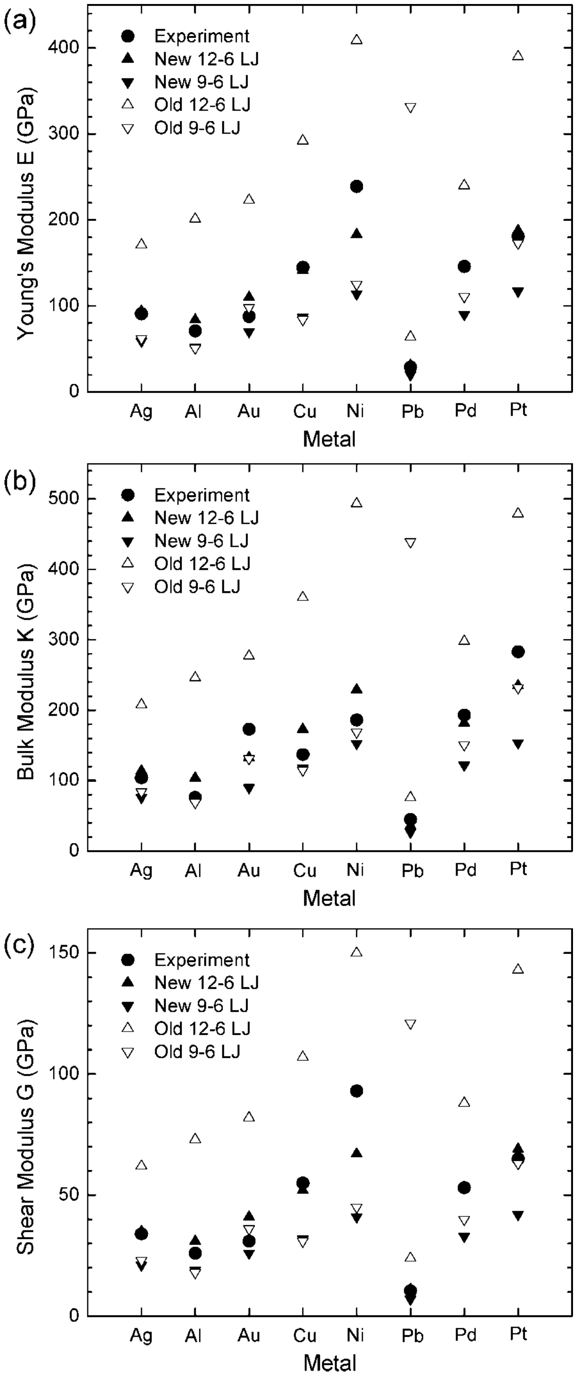

Figure 7. Elastic moduli of the fcc metals according to experiment, the new LJ model, and existing LJ models. (a) Young's modulus, (b) bulk modulus, (c) shear modulus. The 12−6 potential yields overall a good fit, while the 9−6 potential leads to moduli by one-third lower than in experiment.

relative to experiment.[57,58] The difference between computation and experiment amounts to ca. −14% with the 12−6 potential and −8% with the 9−6 LJ potential (Table 4). Attractive polarization due to mirror charges[51] on the even surfaces contributes approximately +0.10 ± 0.05 mJ/m^2, or 5−15% of the interface tension, as will be explained in a separate work. Thus, polarization might be the dominant contribution to offset the gap between computed and experimental interface tensions.[27,28] Other contributions to the difference arise from empirical assumptions in the force field and combination rules of the LJ parameters. Similar trends are expected for interfaces with biological and organic molecules which possess surface and interface properties on a similar scale as water that are in contrast to the very high surface and interface energies of metals.

Overall, the computation of interface tensions is nearly quantitative and provides first evidence that meaningful simulations of interfacial interactions in metal-containing hybrid materials are feasible. The compatibility of the LJ model with widely used force fields allows semiquantitative simulations of metal−organic and metal−biological interfaces, and expected errors in interfacial thermodynamic properties are on the order of 10% vs deviations on the order of 100% with previous LJ models. In comparison to tight binding and density functional methods, the LJ models do not take electronic structure explicitly into account and cannot be applied to chemical reactions at the interface. Nevertheless, essential features of the electronic structure are implicitly included so that computed interfacial energies are of the same accuracy as with quantum mechanical methods.[19] A major advantage is that computation times are about 10^6 times shorter compared to ab initio methods and larger systems up to 10^6 atoms can be simulated at time scales close to microseconds. In comparison to EAM models with 50% deviation in interfacial energies, the LJ models are also clearly more accurate and computation times are at least 10^2 times shorter.

Figure 6 illustrates visually the significance of accurate LJ parameters for a nonoxidized Pb−water interface using the new and the existing 9−6 LJ potential. The new parameters (Figure 6a) reflect the ductility and deformability of lead (low melting point) through significant oscillation of the atoms off the lattice points in comparison with the existing model which displays only minor oscillations of the atoms and a high stiffness due to a highly overestimated surface tension (Figure 6b). The metal interface with water molecules displays weak layering and surface freezing in the accurate new model (Figure 6a), whereas strong layering and surface freezing of water is observed in the existing model with multiple times overestimated surface energy (Figure 6b).

5.4. Elastic Moduli. Computed isotropic elastic properties (Table 5, Figure 7) are in good qualitative agreement with experiment.[46,53] The 12−6 LJ potential achieves quantitative (Pd, Ag) to good qualitative agreement with experiment with typical deviations of ±20% in elastic moduli. The 9−6 LJ potential leads to systematic, fairly uniform underestimates of elastic moduli by approximately −35%. The agreement of computed Poisson ratios with experiment is near quantitative using both models. Experimental Poisson ratios ν for the fcc metals range between 0.29 and 0.42, while the LJ potentials consistently yield ν close to 0.36 in the 12−6 form and close to 0.37 in the 9−6 form (Table 5). The agreement of computed elastic moduli with experiment increases when $\nu_{\mathrm{LJ}} \approx \nu_{\mathrm{metal}}$. Overall, the difference between the 12−6 LJ potential and the 9−6 LJ potential suggests a better suitability of the 12−6 LJ potential to describe mechanical responses of metals and related hybrid interfaces. Even though quantitative agreement with experiment is hardly achieved, the improvement of the new LJ parameters compared to earlier LJ models is remarkable, demonstrated by the reduction of the significant scatter including overestimates of elastic moduli up to several hundred percent as well as underestimates (Figure 7). The increased reliability is primarily associated with the reproduction of surface tensions as one of two reference points for each metal in the parametrization of the new LJ model (section 2.2).

It is also noteworthy that absolute agreement between experimental values among different sources cannot be reached although the discrepancies do not exceed 5%.[35] We refer to commonly accepted values of the elastic constants C_{11}, C_{12}, C_{44}[46,53] and elastic moduli E, K, G, ν in experiment (Table 5 and Figure 7).[53] In this context, it is useful to recall that fcc metals can be considered as isotropic elastic solids.[52,53] Thus, (1) the bulk modulus is obtained as $K = (C_{11} + 2C_{12})/3$, (2) the shear modulus is given as a Voigt average of a single crystal over all space $G = (C_{11} - C_{12} + 3C_{44})/5$, (3) the Poisson ratio follows as $\nu = (3K - 2G)/(6K + 2G)$, and (4) Young's modulus amounts to $E = 9KG/(3K + G)$.[52,53] Only two of the four values E, K, G, and ν are independent from each other, and similar useful relations such as $K = E/[3(1 - 2\nu)]$ and $G = E/(2 + 2\nu)$ between the isotropic elastic constants can be employed.

The new LJ model performs comparable to tight-binding models, which are associated with ~20% deviations in elastic moduli.[19] Significantly lower deviations of only ~1% relative to experiment can be achieved using EAM potentials which include additional adjustable parameters to fit the elastic constants.[20−22] In contrast, many-body potentials without additional terms to fit elastic constants have resulted in more than 100% deviation.[27] Therefore, the reliability of elastic constants in the 12−6 LJ model is indeed very good (in the 9−6 LJ model, acceptable), taking into account the simplicity, high computational efficiency, and compatibility with inorganic as well as (bio)organic force fields.

6. Conclusions

We have developed 12−6 and 9−6 LJ parameters for the simulation of metals and hybrid interfaces with organic, inorganic, and biological compounds. Densities, surface energies, interface energies, as well as mechanical properties are computed in good agreement with experiment under ambient conditions, with average deviations of 0.1, 3, 10, and 25%, respectively. The parameters are developed for room temperature and atmospheric pressure and valid in a 298 ± 200 K range, with the possibility of adjustments for significantly different conditions.[47] The compatibility of the LJ parameters for fcc metals with existing biomolecular and materials-oriented force fields using standard combination rules has been initially demonstrated through the near-quantitative computation of metal−water interface tensions using two force fields with different combination rules. The new LJ models for fcc metals can be implemented in force fields such as AMBER, CHARMM, COMPASS, CVFF, OPLS-AA, PCFF, and applied to the simulation of metals and their interfaces with water, biopolymers, organic molecules, and inorganic components.

The LJ models for fcc metals are typically an order of magnitude more accurate than previous LJ parameters due to the physical interpretation of the quantities r_0 and ε_0 in terms of the metal density and the surface tension of the {111} crystal face under standard conditions. Anticipated deviations in interfacial thermodynamic properties from experiment amount to only ~10% in comparison to ~100% with earlier LJ models. The model is computationally very efficient and easy to implement in Monte Carlo and molecular dynamics simulations due to its simplicity. In comparison with embedded atom and tight-binding models, the LJ potential is of comparable accuracy and computationally up to a million times faster. We find that 12−6 LJ parameters are somewhat preferable over 9−6 parameters for the metals due to better performance in the computation of mechanical properties.

Notably, the models perform well in the computation of quantities they were not originally fitted to. The surface energy anisotropy between the {100} and the {111} metal faces is computed in good agreement with experiment and appears to be related to the geometry of the crystal faces. Elastic properties are computed in good qualitative agreement with experiment which appears to be a consequence of the exact representation of solid−vapor interface tensions under ambient conditions.

The focus of this work has been the derivation and initial validation of the LJ model for fcc metals. Further evaluation of the compatibility with force fields is currently under way, including estimates of polarization on the metal surface as well as the analysis of the adsorption of amino acids and peptides on metal surfaces in aqueous solution.

Acknowledgment. A patent application has been filed by the University of Akron. We are grateful for support from the Air Force Research Laboratory (AFRL) and the University of Akron. Helpful discussions with Ruth Pachter, AFRL, Gustavo Carri and Jutta Luettmer-Strathmann, University of Akron, as well as Tanja Schilling, University of Mainz, Germany, are acknowledged.

References and Notes

(1) Naik, R. R.; Stringer, S. J.; Agarwal, G.; Jones, S. E.; Stone, M. O. *Nat. Mater.* **2002**, *1*, 169–172.

(2) Murphy, C. J.; Sau, T. K.; Gole, A. M.; Orendorff, C. J.; Gao, J.; Gou, L.; Hunyadi, S. E.; Li, T. *J. Phys. Chem. B.* **2005**, *109*, 13857–13870.

(3) Slocik, J.; Naik, R. R. *Adv. Mater.* **2006**, *18*, 1988–1992.

(4) Chen, J.; Wiley, B. J.; Xia, Y. *Langmuir* **2007**, *23*, 4120–4129.

(5) Slocik, J. M.; Tam, F.; Halas, N. J.; Naik, R. R. *Nano Lett.* **2007**, *7*, 1054–1058.

(6) Willett, R. L.; Baldwin, K. W.; West, K. W.; Pfeiffer, L. N. *Proc. Natl. Acad. Sci. USA* **2005**, *102*, 7817–7822.

(7) Sarikaya, M.; Tamerler, C.; Jen, A. K. Y.; Schulten, K.; Baneyx, F. *Nat. Mater.* **2003**, *2*, 577–585.

(8) Heinz, H.; Vaia, R. A.; Farmer, B. L. *Langmuir* **2008**, *24*, 3727–3733.

(9) Leontidis, E.; Heinz, H.; Palewska, K.; Wallenborn, E.-U.; Suter, U. W. *J. Chem. Phys.* **2001**, *114*, 3224–3235.

(10) Heinz, H.; Paul, W.; Suter, U. W.; Binder, K. *J. Chem. Phys.* **2004**, *120*, 3847–3854.

(11) Heinz, H.; Suter, U. W. *Angew. Chem., Int. Ed.* **2004**, *43*, 2239–2243.

(12) Heinz, H.; Paul, W.; Binder, K. *Phys. Rev. E* **2005**, *72*, 066704: 1−10.

(13) Heinz, H.; Koerner, H.; Vaia, R. A.; erson, K. L.; Farmer, B. L. *Chem. Mater.* **2005**, *17*, 5658–5669.

(14) Pandey, R. B.; erson, K. L.; Heinz, H.; Farmer, B. L. *J. Polym. Sci., Part B* **2005**, *43*, 1041–1046.

(15) Jacobs, J. D.; Koerner, H.; Heinz, H.; Farmer, B. L.; Mirau, P. A.; Garrett, P. H.; Vaia, R. A. *J. Phys. Chem. B* **2006**, *110*, 20143–20157.

(16) Schravendijk, P.; Ghiringhelli, L. M.; Delle Site, L.; van der Vegt, N. F. A. *J. Phys. Chem. C* **2007**, *111*, 2631–2642.

(17) Heinz, H.; Vaia, R. A.; Krishnamoorti, R.; Farmer, B. L. *Chem. Mater.* **2007**, *19*, 59–68.

(18) Needs, R. J.; Mansfield, M. *J. Phys.: Condens. Matter* **1989**, *1*, 7555–7563.

(19) Mehl, M. J.; Papaconstantopoulos, D. A. *Phys. Rev. B* **1996**, *54*, 4519–4530.

(20) Baskes, M. I.; Melius, C. F. *Phys. Rev. B* **1979**, *20*, 3197–3204.

(21) Daw, M. S.; Foiles, S. M.; Baskes, M. I. *Mater. Sci. Rep.* **1992**, *9*, 251–310.

(22) Baskes, M. I. *Phys. Rev. Lett.* **1999**, *83*, 2592–2595.

(23) Born, M. *Verh. Dtsch. Phys. Ges.* **1919**, *21*, 13–24.

(24) Jones, J. E. *Proc. R. Soc. London, Ser. A* **1924**, *106*, 463–477.

(25) Jones, J. E.; Ingham, A. E. *Proc. R. Soc. London, Ser. A* **1925**, *107*, 636–653.

(26) Shu, Z.; Davies, G. J. *Phys. Status Solidi A* **1983**, *78*, 595–605.

(27) Uppenbrink, J.; Wales, D. J. *J. Chem. Phys.* **1992**, *96*, 8520–8534.

(28) Dauber-Osguthorpe, P.; Roberts, V. A.; Osguthorpe, D. J.; Wolff, J.; Genest, M.; Hagler, A. T. *Proteins: Struct., Function Genetics* **1988**, *4*, 31–47.

(29) (a) Maple, J. R.; Thacher, T. S.; Dinur, U.; Hagler, A. T. *Chem. Des. Autom. News* **1990**, *5*, 5–10. (b) Sun, H.; Mumby, S. J.; Maple, J. R.; Hagler, A. T. *J. Am. Chem. Soc.* **1994**, *116*, 2978–2987. (c) Sun, H. *J. Comput. Chem.* **1994**, *15*, 752–768. (d) Hill, J.-R.; Sauer, J. *J. Phys. Chem.* **1994**, *98*, 1238–1244. (e) Sun, H. *Macromolecules* **1995**, *28*, 701–712.

(30) Pearlman, D. A.; Case, D. A.; Caldwell, J. W.; Ross, W. S.; Cheatham, T. E.; DeBolt, S.; Ferguson, D.; Seibel, G.; Kollman, P. *Comput. Phys. Commun.* **1995**, *91*, 1–41.

(31) Jorgensen, W. L.; Maxwell, D. S.; Tirado-Rives, J. *J. Am. Chem. Soc.* **1996**, *118*, 11225–11236.

(32) MacKerell, A. D., Jr.; Bashford, D.; Bellott, R. L.; Dunbrack, R. L., Jr.; Evanseck, J. D.; Field, M. J.; Fischer, S.; Gao, J.; Guo, H.; Ha, S.; Joseph-McCarthy, D.; Kuchnir, L.; Kuczera, K.; Lau, F. T. K.; Mattos, C.; Michnick, S.; Ngo, T.; Nguyen, D. T.; Prodhom, B.; Reiher, W. E., III; Roux, B.; Schlenkrich, M.; Smith, J. C.; Stote, R.; Straub, J.; Watanabe, M.; Wiorkiewicz-Kuczera, J.; Yin, D.; Karplus, M. *J. Phys. Chem. B* **1998**, *102*, 3586–3616.

(33) Sun, H. *J. Phys. Chem. B* **1998**, *102*, 7338–7364.

(34) Materials Studio 4.0, Cerius2, InsightII, and Discover programs, Accelrys, Inc., 2006.

(35) Hirschfelder, J. O.; Curtiss, C. F.; Bird, R. B. *Molecular Theory of Gases and Liquids*; Wiley: New York, 1954.

(36) Heinz, H.; Suter, U. W.; Leontidis, E. *J. Am. Chem. Soc.* **2001**, *123*, 11229–11236.

(37) Heinz, H.; Castelijns, H. J.; Suter, U. W. *J. Am. Chem. Soc.* **2003**, *125*, 9500–9510.

(38) Marrone, T. J.; Merz, K. M. *J. Phys. Chem.* **1993**, *97*, 6524–6529.

(39) Aqvist, J. *J. Phys. Chem.* **1994**, *98*, 8253–8255.

(40) Merz, K. M. *J. Phys. Chem.* **1994**, *98*, 8256–8257.

(41) Delhommelle, J.; Millie, P. *Mol. Phys.* **2000**, *99*, 619–625.

(42) Chen, A. A.; Pappu, R. V. *J. Phys. Chem. B* **2007**, *111*, 11884–11887.

(43) Nath, S.; Escobedo, F. A.; de Pablo, J. J. *J. Chem. Phys.* **1998**, *108*, 9905–9911.

(44) Virnau, P.; Muller, M.; MacDowell, L. G.; Binder, K. *J. Chem. Phys.* **2004**, *121*, 2169–2179.

(45) Tyson, W. R.; Miller, W. A. *Surf. Sci.* **1977**, *62*, 267–276.

(46) *CRC Handbook of Chemistry and Physics*; 84th ed.; Lide, D. R., Ed.; CRC Press: Boca-Raton, 2003.

(47) Higher temperatures typically leads to an increase in ε_0. A first guess of the new parameters at a temperature T_2 relative to the initial temperature T_1 can be obtained from the experimental cell parameters $a(T_1)$, $a(T_2)$, and the experimental surface tensions $\gamma_{SV}^{\{111\}}(T_1)$, $\gamma_{SV}^{\{111\}}(T_2)$ at both temperatures[45,46] using $r_0(T_2) = r_0(T_1)a(T_2)/a(T_1)$ and $\varepsilon_0^{\{\}}(T_2) = \varepsilon_0^{\{\}}(T_1)\gamma_{SV}^{\{111\}}(T_2)/\gamma_{SV}^{\{111\}}(T_1)$, followed by exact refinement.

(48) Heinz, H.; Vaia, R. A.; Farmer, B. L. *J. Chem. Phys.* **2006**, *124*, 224713:1–9.

(49) The entropy contribution to thesurface tension can be estimated on the basis of the melting entropy which amounts to approximately $\Delta S_m = 1.0k$ for fcc metals.[46] If the first layer of metal atoms on the {111} surface would gain unrestricted translational freedom upon cleavage ($N = 56$ atoms cover a cross-sectional area A of ~4 nm^2), the entropy contribution lowers the surface energy by$-T\Delta S/A = -NkT/A = -55$ mJ/m^2 at 298 K. The simulation, however, shows almost no increase in translational freedom upon cleavage (except for Pb, where a modest gain is visible) so that we assume the entropy correction to be less than-0.01 J/m^2 (Fig. 3). This uncertainty is small compared to surface tensions of metals in the range 0.5−2.5 J/m^2 (ref 45) and essentially within the standard deviation of experimental measurements (≥ 0.01 J/m^2).

(50) Heinz, H. *Mol. Sim.* **2007**, *33*, 747–758.

(51) Guidelli, R.; Schmickler, W. *Electrochim. Acta* **2000**, *45*, 2317–2338.

(52) Kosevich, A. M.; Lifshitz, E. M.; Landau, L. D.; Pitaevskii, L. P. *Theory of Elasticity*, 3rd ed.; Landau, L. D.; Butterworth-Heinemann, Oxford, 1999; Vol. 7.

(53) Simmons, G.; Wang, H. *Single Crystal Elastic Constants and Calculated Aggregate Properties: A Handbook*, 2nd ed.; MIT Press: Cambridge, MA, 1971.

(54) Plimpton, S. J. *J. Comp. Phys.* **1995**, *117*, 1–19. See also: www.lammps.sandia.gov.

(55) The identity of PCFF parameters and COMPASS parameters for the eight metals under consideration was shown using single point energy calculations. Numerical equivalence of the energies using PCFF and COMPASS was found up to all post-comma digits for arbitrary assemblies of atoms.

(56) (a) Menon, S. K.; Martin, P. L. *Ultramicroscopy* **1986**, *20*, 93–98. The authors explain that the particle shape in earlier studies of the surface energy anisotropy was influenced by substrate−condensate interactions. Thus, ratios between the {110} and {111} surface tensions of 1.03−1.15 in earlier reports actually range from 1.01 to 1.04 for {100} vs {111} surfaces and for {110} vs {111} surfaces when such interferences are eliminated. (b) Flueli, M.; Borel, J. P. *J. Cryst. Growth* **1988**, *91*, 67–70. Ratios between the {100} and the {111} surface energy for Au near 1.05 are reported. (c) Lee, W. H. Vanloon; K, R.; Petrova, V.; Woodhouse, J. B.; Loxton, C. M.; Masel, R. I. *J. Catal.* **1990**, *126*, 658–671. The relative energy of Pt {100} and {111} surfaces was examined under oxidative conditions (O_2) at high temperatures. While stepped surfaces and {100} surfaces were preferred under these particular conditions, relative energy differences between {100} and {111} faces are generally identified as ~4%. (d) Girin, O. B.; Vorob'ev, G. M. *Russian Metallurgy* **1992**, *6*, 90–98. A broken bond model is employed to derive generic surface energy anisotropies in fcc metals. The resulting the ratio of 1.106 for {100} vs {111} surface tensions, however, appears too high in comparison to experiment.

(57) Osman, M. A.; Keller, B. A. *Appl. Surf. Sci.* **1996**, *99*, 261–263.

(58) Experimental value for the metal−water interface tension γ^{SL} are obtained from the Young equation $\gamma^{SL} + \gamma^{LV} \cos \theta = \gamma^{SV}$ using contact angles θ of water and of nonpolar solvents on clean metal surfaces of 0°.[57] Accordingly, γ^{SL} is given by the metal−vapor surface tension γ^{SV} (Table 3) and the surface tension of water $\gamma^{LV} = 73$ mJ/m^2 (ref 46) by the relation $\gamma^{SL} = \gamma^{SV} - \gamma^{LV}$.

JP801931D